Migration velocity analysis for anisotropic models

Yunyue (Elita) Li and Biondo Biondi**

SUMMARY

Anisotropic models are recognized as a more realistic representation of the subsurface where complex geological environment exists. These models are widely needed by all kinds of migration and interpretation schemes. However, anisotropic model building is still a challenging problem in the industry. In this paper, we propose an approach to building anisotropic models from surface seismic data based on the theory of Wave-Equation Migration Velocity Analysis (WEMVA). Because of the ambiguity between depth and δ, we parametrize our model space using only NMO velocity (V_{nmo}) and the anellipticity parameter η. We present a synthetic data example of anisotropic WEMVA applied to the shallow part of the Hess anisotropic synthetic VTI model. The results show that anisotropic WEMVA is effective in resolving the anisotropic perturbation; however, a unique solution to the inversion requires additional constraining information.

INTRODUCTION

Since first reported in exploration seismology in the 1930s (McCollum and Snell, 1932), anisotropy has become increasingly important in seismic imaging and exploration. Until now, the transverse isotropic (TI) model has been the most commonly used in seismic imaging. Postma (1955) and Helbig (1956) showed that a sequence of isotropic layers on a scale much smaller than the wavelength leads to an anisotropic medium. If the layers are horizontal, the medium is defined as a vertical TI (VTI) medium. A VTI medium is commonly formed because of the thin bedding during the deposition. If the layers become dipping during the deformation, a tilted TI (TTI) medium is formed. Many authors (Shan, 2009; Fletcher et al., 2009; Zhang and Zhang, 2009; Fei and Liner, 2008) have developed migration and processing schemes for VTI and TTI media; however, the challenge of estimating the anisotropy model remains the bottleneck for the exploration workflow.

The existing anisotropic model-building schemes are mostly based on measuring the non-hyperbolic moveout along the traveltime curve to flatten the common image gathers (CIG) (Zhou et al., 2003, 2004; Yuan et al., 2006; Cai et al., 2009). However, traveltime ray-based methods are prone to errors and unrealistic results when multi-pathing exists in areas of complex overburden. Hence, we propose to apply Wave-Equation Migration Velocity Analysis (WEMVA) for anisotropic model building.

WEMVA has been widely studied in isotropic velocity building and can be implemented either in the data space (Tarantola, 1984; Woodward, 1992) or in the image space (Sava and Biondi, 2004a,b; Shen, 2004; Shen and Symes, 2008; Guerra et al., 2009). Several advantages drive us to use the image-space WEMVA instead of data-space WEMVA (Full-Waveform Inversion): first, the migrated image is often much cleaner than the recorded wavefields; second, the objective function is directly related to the final image. Therefore, we choose to extend image-space WEMVA from isotropic velocity building to anisotropic model building.

In this paper, we first generalize the methodology of image-space WEMVA from an isotropic medium to an anisotropic medium and explain our parameterization. We show that theoretically the gradient of the tomographic objective functional for an isotropic medium can be modified to describe an anisotropic medium by simply adding a term for additional parameters. Finally, we test our inversion scheme on a shallow part of the Hess anisotropic synthetic dataset.

MIGRATION VELOCITY ANALYSIS FOR ANISOTROPIC PARAMETERS

Anisotropic MVA is a non-linear inversion process that aims to find the background anisotropic model that minimizes the residual field $\Delta\mathbf{I}$ in the image space. The residual image is derived from the background image $\mathbf{I}$, which is computed with current background model. To form the image, both the source and receiver wavefields are downward continued using the one-way wave equations in the shot-profile domain. Assuming that the shear velocity is much smaller than the P-wave velocity, one way of formulating up-going and down-going one-way acoustic wave equations for VTI is shown as follows (Shan, 2009):

$$\left(\frac{\partial}{\partial z} \mp i\Lambda\right) P = 0, \tag{1}$$

where $P = P(x,y,z,\omega)$ is the wavefield in the space-frequency domain and Λ discribes the dispersion relationship in terms of P-wave vertical slowness s_0 and Thomsen parameters ε and δ (Thomsen, 1986):

$$\Lambda = \omega s_0 \sqrt{\frac{\omega^2 s_0^2 - (1+2\varepsilon)|\mathbf{k}|^2}{\omega^2 s_0^2 - 2(\varepsilon-\delta)|\mathbf{k}|^2}}, \tag{2}$$

where $\mathbf{k} = (k_x, k_y)$ is the spatial wavenumber vector.

Many authors (Tsvankin and Thomsen, 1994; Alkhalifah and Tsvankin, 1995) have shown that P-wave traveltime can be characterized by the NMO slowness, s_n, and the anellipticity parameter η. Therefore, the one-way wave-equation in terms of s_n, η and δ is:

$$\left(\frac{1}{\sqrt{1+2\delta}}\frac{\partial}{\partial z} \mp i\Lambda'\right) P = 0 \tag{3}$$

where

$$\Lambda' = \omega s_n \sqrt{1 - \frac{|\mathbf{k}|^2}{\omega^2 s_n^2 - 2\eta|\mathbf{k}|^2}}. \tag{4}$$

Notice that in the dispersion relationship in Equation 3, δ and the derivative in depth $\frac{\partial}{\partial z}$, are coupled with each other. This

is a thoeretical proof of the well-accepted observation that δ cannot be determined by the surface seismic data. To constrain this parameter, we need well information to add the depth dimension into the inversion.

Now, if we apply the change of variables

$$d\bar{z} = \sqrt{1+2\delta}dz \tag{5}$$

and neglect the derivatives of δ, Equation 3 becomes

$$\left(\frac{\partial}{\partial \bar{z}} \mp i\Lambda'\right) P = 0. \tag{6}$$

Therefore, we formulate the image-space migration velocity analysis problem with NMO slowness s_n and anisotropic parameters η and δ, but we invert only for s_n and η.

Notice that when $\eta = 0$, dispersion relationship (Equation 4) is the same as the isotropic dispersion relationship, and the corresponding one-way wave equation (Equation 6) is almost the same as for the isotropic case except for a depth stretch caused by δ. This is to say an elliptic anisotropic wavefield inversion is almost equivalent to an isotropic wavefield inversion. Plessix and Rynja (2010) demostrated the same conclusions for full-waveform inversion (FWI). Figure 1 compares the original NMO velocity to the streched NMO velocity. Notice that the geological features are stretched downward for positive δ. Because we ignore δ in the inversion, we expect the inverted NMO velocity to be more similar to the stretched NMO velocity than to the original one.

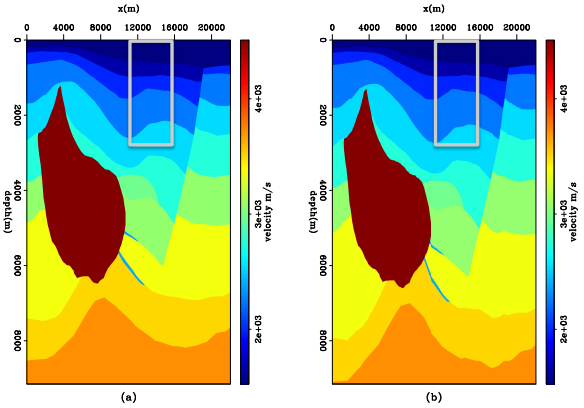

Figure 1: (a) Original NMO velocity for the anisotropic Hess model; (b) Stretched NMO velocity according to δ.

In general, the residual image is defined as (Biondi, 2008)

$$\Delta\mathbf{I} = \mathbf{I} - \mathbf{F}(\mathbf{I}), \tag{7}$$

where $\mathbf{F}$ is a focusing operator. In the least-square sense, the tomographic objective function can be written as follows:

$$J = \frac{1}{2}||\Delta\mathbf{I}||_2 = \frac{1}{2}||\mathbf{I} - \mathbf{F}(\mathbf{I})||^2. \tag{8}$$

To perform MVA for anisotropic parameters, we first need to extend the tomographic operator from the isotropic medium (Shen, 2004; Sava, 2004; Guerra et al., 2009) to the anisotropic medium. We define the wave-equation tomographic operator $\mathbf{T}$ for anisotropic models as follows:

$$\begin{aligned}\mathbf{T} &= \left.\frac{\partial \mathbf{I}}{\partial \mathbf{m}}\right|_{\mathbf{m}=\widehat{\mathbf{m}}} \\ &= \left.\frac{\partial \mathbf{I}}{\partial \mathbf{s_n}}\right|_{\mathbf{s_n}=\widehat{\mathbf{s_n}}} + \left.\frac{\partial \mathbf{I}}{\partial \eta}\right|_{\eta=\widehat{\eta}}\end{aligned} \tag{9}$$

where $\mathbf{m}$ is the anisotropy model, which in this case includes NMO slowness $\mathbf{s_n}$ and aellipticity parameter η; $\widehat{\mathbf{m}}$ is the background anisotropy model, consisting of the background NMO slowness $\widehat{\mathbf{s_n}}$ and background aellipticity $\widehat{\eta}$; and $\mathbf{I}$ is the image.

This wave equation tomographic operator $\mathbf{T}$ is a linear operator that relates the model perturbation $\Delta\mathbf{m}$ to the image perturbation $\Delta\mathbf{I}$ as follows:

$$\Delta\mathbf{I} = \mathbf{T}\Delta\mathbf{m}. \tag{10}$$

In the shot-profile domain, both source and receiver wavefields are downward continued using the one-way wave equation (Equation 6):

$$\begin{cases} \left(\frac{\partial}{\partial z} + i\Lambda'\right) D(\mathbf{x},\mathbf{x}_s) = 0 \\ D(x,y,z=0,\mathbf{x}_s) = f_s\delta(\mathbf{x}-\mathbf{x}_s) \end{cases}, \tag{11}$$

and

$$\begin{cases} \left(\frac{\partial}{\partial z} + i\Lambda'\right) U(\mathbf{x},\mathbf{x}_s) = 0 \\ U(x,y,z=0,\mathbf{x}_s) = Q(x,y,z=0,\mathbf{x}_s) \end{cases}, \tag{12}$$

where $D(\mathbf{x},\mathbf{x}_s)$ is the source wavefield at the image point $\mathbf{x} = (x,y,z)$ with the source located at $\mathbf{x}_s = (x_s,y_s,0)$; $U(\mathbf{x},\mathbf{x}_s)$ is the receiver wavefield at the image point $\mathbf{x}$ with the source located at $\mathbf{x}_s$; f_s is the source signature, and $f_s\delta(\mathbf{x}-\mathbf{x}_s)$ defines the point source function at $\mathbf{x_s}$, which serves as the boundary condition of Equation 11; and $Q(x,y,z=0,\mathbf{x}_s)$ is the recorded shot gather for the shot located at $\mathbf{x}_s$, which serves as the boundary condition of Equation 12.

The dispersion relationship in Equation 4 can be approximated with a rational function by Taylor series and Padé expansion analysis (Shan, 2009):

$$\Lambda' = \omega s_n \left(1 - \frac{a|\mathbf{k}|^2}{\omega^2 s_n^2 - b|\mathbf{k}|^2}\right), \tag{13}$$

where, to the second order, $a = 0.5, b = 0.25 + 2\eta$. Equation 13 using binomial expansion can be further expanded to polynomials:

$$\Lambda' = \omega s_n - \frac{a}{\omega^2 s_n^2}|\mathbf{k}|^2 - \frac{ab}{\omega^4 s_n^4}|\mathbf{k}|^4. \tag{14}$$

Now it is trivial to take the derivative of Λ' with respect to s_n and η.

The background image is computed by applying the cross-correlation imaging condition:

$$I(\mathbf{x},\mathbf{h}) = \sum_{\mathbf{x}_s}\sum_{\omega} \overline{D(\mathbf{x}-\mathbf{h},\mathbf{x}_s)}U(\mathbf{x}+\mathbf{h},\mathbf{x}_s), \tag{15}$$

where the overline stands for complex conjugate, and $\mathbf{h} = (h_x,h_y,h_z)$ is the subsurface half-offset.

Perturbing the wavefields in Equation 15 and ignoring the higher-order term, we can get the perturbed image as follows:

$$\Delta I(\mathbf{x},\mathbf{h}) = \sum_{\mathbf{x}_s}\sum_{\omega}\Big(\overline{\Delta D(\mathbf{x}-\mathbf{h},\mathbf{x}_s)}\widehat{U}(\mathbf{x}+\mathbf{h},\mathbf{x}_s)+ \overline{\widehat{D}(\mathbf{x}-\mathbf{h},\mathbf{x}_s)}\Delta U(\mathbf{x}+\mathbf{h},\mathbf{x}_s)\Big), \quad (16)$$

where $\widehat{D}(\mathbf{x}-\mathbf{h},\mathbf{x}_s)$ and $\widehat{U}(\mathbf{x}+\mathbf{h},\mathbf{x}_s)$ are the background source and receiver wavefields computed with the background model $\widehat{m}(\mathbf{x})$; and $\Delta D(\mathbf{x}-\mathbf{h},\mathbf{x}_s)$ and $\Delta U(\mathbf{x}+\mathbf{h},\mathbf{x}_s)$ are the perturbed source wavefield and perturbed receiver wavefield, which are the results of the model perturbation $\Delta m(\mathbf{x})$.

To evaluate the adjoint tomographic operator $\mathbf{T}^*$, which maps from the image perturbation to the model perturbation, we first compute the wavefield perturbation from the image perturbation using the adjoint imaging condition:

$$\begin{aligned}\Delta D(\mathbf{x},\mathbf{x}_s) &= \sum_{\mathbf{h}}\Delta I(\mathbf{x},\mathbf{h})\widehat{U}(\mathbf{x}+\mathbf{h},\mathbf{x}_s)\\ \Delta U(\mathbf{x},\mathbf{x}_s) &= \sum_{\mathbf{h}}\Delta I(\mathbf{x},\mathbf{h})\widehat{D}(\mathbf{x}-\mathbf{h},\mathbf{x}_s).\end{aligned} \quad (17)$$

The perturbed source and receiver wavefields satisfy the following one-way wave equations, linearized with respect to NMO slowness and η:

$$\begin{cases}\left(\frac{\partial}{\partial z}+i\Lambda'\right)\Delta D(\mathbf{x},\mathbf{x}_s)=\left(-i\frac{\partial\Lambda'}{\partial\mathbf{m}}\widehat{D}(\mathbf{x},\mathbf{x}_s)\right)\Delta\mathbf{m}^*(\mathbf{x})\\ \Delta D(x,y,z=0,\mathbf{x}_s)=0\end{cases}, \quad (18)$$

and

$$\begin{cases}\left(\frac{\partial}{\partial z}+i\Lambda'\right)\Delta U(\mathbf{x},\mathbf{x}_s)=\left(-i\frac{\partial\Lambda'}{\partial\mathbf{m}}\widehat{U}(\mathbf{x},\mathbf{x}_s)\right)\Delta\mathbf{m}^*(\mathbf{x})\\ \Delta U(x,y,z=0,\mathbf{x}_s)=0\end{cases}. \quad (19)$$

where $\mathbf{m}$ is the row vector $[\mathbf{s_n}\ \eta]$.

During the inversion, the model perturbation is unkown, and in fact must be estimated. Therefore, we obtain the image perturbation by applying a focusing operator (Equation 7) to the current background image. Then the perturbed image is convolved with the background wavefields to get the perturbed wavefields (Equation 17). The scattered wavefields are obtained by applying the adjoint of the one-way wave-equations 18 and 19. Finally, the model-space gradient is obtained by cross-correlating the upward propagated scattered wavefields with the modified background wavefields (the terms in the parentheses on the right-hand sides of equations 18 and 19).

OBJECTIVE FUNCTION

As mentioned in the previous section, we estimate the optimum earth model by minimizing a user-defined image perturbation. There are many ways to define the objective function. Here we use the Differential Semblance Optimization (DSO) method (Shen, 2004) as the criterion:

$$\mathbf{F}(\mathbf{I}) = (\mathbf{1}-\mathbf{O})\mathbf{I}, \quad (20)$$

where $\mathbf{1}$ is the identity operator and $\mathbf{O}$ is the differential operator along the angle axes in the ADCIGs. In the subsurface-offset domain, the objective function (Equation 8) reads:

$$J = \frac{1}{2}||h\mathbf{I}(\mathbf{x},h)||_2, \quad (21)$$

where h is the subsurface-offset, and $\mathbf{I}(\mathbf{x},h)$ is the image gather in the subsurface-offset domain. This operator is preferred by many researchers since it is a fully automated procedure, with no picking required. However, for isotropic migration velocity analysis, many authors (Vyas and Tang, 2010; Fei and Williamson, 2010) observe undesired artifacts generated by the DSO operator and suggest that a differential operator along h can help compensate for the phaseshift caused by the velocity perturbation. Therefore, we use the modified DSO operator as follows:

$$J = \frac{1}{2}||h\mathbf{D}\mathbf{I}(\mathbf{x},h)||_2, \quad (22)$$

where $\mathbf{D}$ is a differential operator in h. Taking the derivative in the subsurface offset domain is equivalent to an α weighting in the angle domain. Therefore, the objective function (Equation 22) also emphasizes the contribution of the large angle information, which is crucial for velocity analysis.

To regularize the inversion, we smooth the gradient using B-spline operator. The smoothed gradient is formulated as:

$$\hat{\mathbf{g}} = \mathbf{B}\mathbf{B}^*\mathbf{g}, \quad (23)$$

where $\mathbf{g}$ and $\hat{\mathbf{g}}$ are the original and the smoothed gradient, respectively; $\mathbf{B}$ is the B-spline projection operator. Then the spacing of the B-spline nodes controls the smoothness of the model update. Practically, we can choose different B-spline parameters for velocity and η.

NUMERICAL TEST

We test our inversion scheme on the shallow part of the Hess synthetic anisotropic model, as denoted by the gray square in Figure 1. The initial model is a 1D gradient isotropic model from the seabed. Figure 2 compares the inversion results with the true models. The ratio of intial velocity and inverted velocity over the true stretched NMO velocity are shown in Figure 2(a) and 2(b), respectively. The inversion successfully reduces the error in velocity from 20% to less than 5%. Notice that the error in velocity generally follows the dip in the image. This suggests that we should use better smoothing operators such as dip filters (Hale, 2007) or steering filters (Clapp, 2000) to regularize the inversion.

On the other hand, the η update (Figure 2(d)) is in general larger than the true η model (Figure 2(c)). A trade-off is observed at depth of 1200m, where the inverted velocity is lower but η is much bigger than the true. This result illustrates the null space of our inversion problem since the reflector around 1200m is well-focused in the inverted image (Figure 3(b)). The higher value of η and the higher velocity in the deeper part of the model explain the smiling event in the subsurface-offset image at depth of 2300m in Figure 3(b). This problem can probably be resolved by increasing the angle coverage at depth and allowing more iterations in the inversion.

Figure 3 compares the subsurface-offset images using the initial model (a), the updated model (b) and the true model (c). After the inversion, the reflectors are focused at zero subsurface-offset, and the depths of the reflectors are closer to the true depths. However, due to the insufficient angle coverage at depth, both the velocity and η are inaccurate. Therefore, the deepest reflector is not perfectly focused in the subsurface-offset domain.

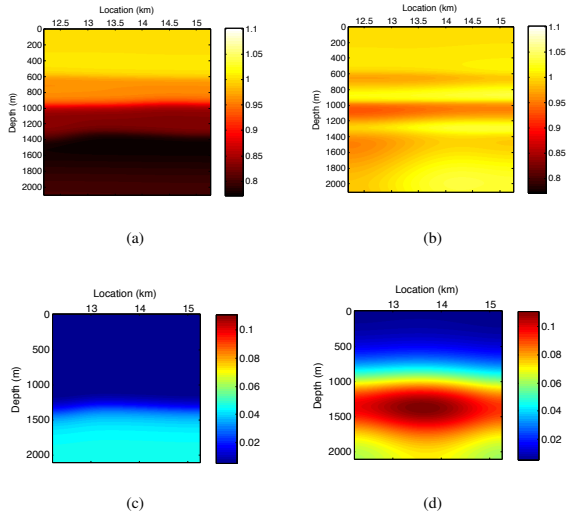

Figure 2: (a) Ratio of initial velocity over true velocity; (b) Ratio of inverted velocity over true velocity; (c) True η model; (d) Inverted η model.

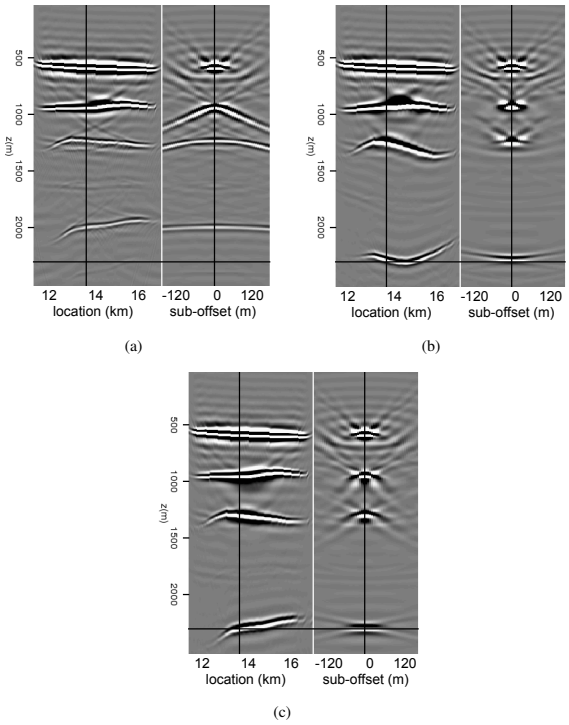

Figure 3: Subsurface offset images using the initial model (a), the updated model (b) and the true model (c).

CONCLUSION AND DISCUSSION

We have presented a new methodology for performing image-domain migration velocity analysis in anisotropic media. Our method is a natural extension of isotropic MVA theory and retains the same properties as the isotropic MVA. We demostrate our method on a 2-D synthetic data set. After inversion, we obtain better-focused subsurface-offset images and better-defined depths. By including the geological information and the wider-offset data, we should be able to eliminate the model error at depth.

Experience shows that the DSO operator has a layer-stripping effect during the iterations. One cause of this effect is the unbalanced amplitude for the reflectors in depth. Therefore, an illumination-corrected image is preferred to compensate for this effect. On the other hand, a residual-moveout-based objective function (Sava, 2004; Sava and Biondi, 2004a,b) could avoid the problem.

Compared with ray-based image-space model-building methods, our wavefield-based image-space method is computationally more intensive. However, the wavefield method better approximates wave propagation in complex areas. We can also utilize the phase-encoded target-oriented image-space wavefield tomography technique to reduce the computational cost.

Finally, by introducing another parameter η into the MVA inversion, we now have a larger model space and hence a larger null space with respect to the same data. Therefore, the surface reflection seismic data is inadequate for resolving a unique earth model. Other information, such as borehole measurement, geological interpretation, and rock physics prior knowledge (Li et al., 2011), is necessary to obtain a consistent, unique and reliable earth model.

ACKNOWLEDGMENT

We would like to thank James Berryman for fruitful discussion about the theory and the choice of the synthetic model. We thank Hess for providing the Hess anisotropic synthetic data set. We thank the sponsors of Stanford Exploration Project for financial support.

EDITED REFERENCES

Note: This reference list is a copy-edited version of the reference list submitted by the author. Reference lists for the 2011 SEG Technical Program Expanded Abstracts have been copy edited so that references provided with the online metadata for each paper will achieve a high degree of linking to cited sources that appear on the Web.

REFERENCES

Alkhalifah, T., and I. Tsvankin, 1995, Velocity analysis for transversely isotropic media: Geophysics, **60**, 1550–1566, doi:10.1190/1.1443888.

Biondi, B., 2008, Automatic wave-equation migration velocity analysis: SEP-134, 65–78.

Cai, J., Y. He, Z. Li, B. Wang, and M. Guo, 2009, TTI/VTI anisotropy parameters estimation by focusing analysis, Part I: Theory: 79th Annual International Meeting, SEG, Expanded Abstracts, 28.

Clapp, R., 2000, Geologically constrained migration velocity analysis: PhD thesis, Stanford University.

Fei, T. W., and C. L. Liner, 2008, Hybrid Fourier, finite-difference 3D depth migration for anisotropic media: Geophysics, **73**, no. 2, S27–S34, doi:10.1190/1.2828704.

Fei, W. and P. Williamson, 2010, On the gradient artifacts in migration velocity analysis based on differential semblance optimization: 80th Annual International Meeting, SEG, Expanded Abstracts, 29.

Fletcher, R., X. Du, and P. J. Fowler, 2009, Stabilizing acoustic reverse-time migration in TTI media: 79th Annual International Meeting, SEG, Expanded Abstracts, 28.

Guerra, C., Y. Tang, and B. Biondi, 2009, Wave-equation tomography using image-space phase-encoded data: SEP Report, **138**, 95.

Hale, D., 2007, Local dip filtering with directional Laplacians: CWP Report 567.

Helbig, K., 1956, Die ausbreitung elastischer Wellen in anisotropen Medien: Geophysical Prospecting, **4**, no. 1, 70–81, doi:10.1111/j.1365-2478.1956.tb01397.x.

Li, Y., D. Nichols, K. Osypov, and R. Bachrach, 2011, Anisotropic tomography using rock physics constraints: Accepted by EAGE.

McCollum, B., and F. Snell, 1932, Asymmetry of sound velocity in stratified formations: Journal of Applied Physics, **2**, no. 3, 174–185, doi:10.1063/1.1745044.

Plessix, R.-E. and H. Rynja, 2010, VTI full-waveform inversion: a parameterization study with a narrow azimuth streamer data example: 80th Annual International Meeting, SEG, Expanded Abstracts, 29.

Postma, G. W., 1955, Wave propagation in a stratified medium: Geophysics, **20**, 780–806, doi:10.1190/1.1438187.

Sava, P., 2004, Migration and velocity analysis by wavefield extrapolation: PhD thesis, Stanford University.

Sava, P., and B. Biondi, 2004a, Wave-equation migration velocity analysis — I: Theory: Geophysical Prospecting, **52**, no. 6, 593–606, doi:10.1111/j.1365-2478.2004.00447.x.

———, 2004b, Wave-equation migration velocity analysis — II: Examples: Geophysical Prospecting, **52**, no. 6, 607–623, doi:10.1111/j.1365-2478.2004.00448.x.

Shan, G., 2009, Optimized implicit finite-difference and Fourier finite-difference migration for VTI media: Geophysics, WCA189–WCA197.

Shen, P., 2004, Wave-equation migration velocity analysis by differential semblance optimization: PhD thesis, Rice University.

Shen, P., and W. W. Symes, 2008, Automatic velocity analysis via shot profile migration: Geophysics, **73**, no. 5, VE49–VE59, doi:10.1190/1.2972021.

Tarantola, A., 1984, Inversion of seismic reflection data in the acoustic approximation: Geophysics, **49**, 1259–1266, doi:10.1190/1.1441754.

Thomsen, L., 1986, Weak elastic anisotropy: Geophysics, **51**, 1954–1966, doi:10.1190/1.1442051.

Tsvankin, I., and L. Thomsen, 1994, Nonhyperbolic reflection moveout in anisotropic media: Geophysics, **59**, 1290–1304, doi:10.1190/1.1443686.

Vyas, M. and Y. Tang, 2010, Gradients for wave-equation migration velocity analysis: 80th Annual International Meeting, SEG, Expanded Abstracts, 29.

Woodward, M. J., 1992, Wave-equation tomography: Geophysics, **57**, 15–26, doi:10.1190/1.1443179.

Yuan, J., X. Ma, S. Lin, and D. Lowrey, 2006, P-wave tomographic velocity updating in 3D inhomogeneous VTI media: 76th Annual International Meeting, SEG, Expanded Abstracts, 25.

Zhang, Y. and H. Zhang, 2009, A stable TTI reverse time migration and its implementation: 79th Annual International Meeting, SEG, Expanded Abstracts, 28.

Zhou, H., D. Pham, and S. Gray, 2004, Tomographic velocity analysis in strongly anisotropic TTI media: 74th Annual International Meeting, SEG, Expanded Abstracts, 23.

Zhou, H., D. Pham, S. Gray, and B. Wang, 2003, 3D tomographic velocity analysis in transversely isotropic media: 73rd Annual International Meeting, SEG, Expanded Abstracts, 22.